

Detecting Landmines With Ground-Penetrating Radar Using Feature-Based Rules, Order Statistics, and Adaptive Whitening

Paul Gader, *Senior Member, IEEE*, Wen-Hsiung Lee, and Joseph N. Wilson

Abstract—An approach to detecting landmines using ground-penetrating radar (GPR) based on feature-based rules, order statistics, and adaptive whitening (FROSAW) is described. FROSAW relies on independent adaptation of whitening statistics in different depths and combining feature-based methods with anomaly detection using rules. Constant false alarm rate (CFAR) detectors are used for anomaly detection on the depth-dependent adaptively whitened data. A single CFAR confidence measure is computed via a function of order statistics. Anomalies are detected at locations with high CFAR confidence. Depth-dependent features are computed on regions containing anomalies. Rules based on the features are used to reject alarms that do not exhibit mine-like properties. The utility of combining the CFAR and feature-based methods is evaluated. The algorithms and analysis are applied to data acquired from tens of thousands of square meters from several outdoor test sites with a state-of-the-art array of GPR sensors.

Index Terms—Adaptive signal detection, constant false alarm rate (CFAR), ground-penetrating radar (GPR), landmine detection, order statistics.

I. INTRODUCTION

LANDMINES have been laid in conflicts around the world, and they continue to maim or kill civilians and soldiers. Detection and removal of land mines is a serious issue to be addressed. Although metal detectors have been successfully used to detect metallic mines, they have difficulty detecting plastic mines or mines that have low metal content. Ground-penetrating radar (GPR) is a high-resolution electromagnetic device that makes amenable the problem of detecting land mines that have little or no metal content.

A variety of systems and algorithms employing GPR sensors have been applied to the problem of landmine detection. The GPR system reported in this paper employs a time-domain pulsed radar sensor. The system employs a vehicle-mounted linear array of transmitter/receiver antennas. In addition, a global positioning system (GPS) provides universal transverse mercator (UTM) coordinates [1] to identify the earth-based position of the sensor array at any time.

A variety of methods have been applied to the problem of detecting landmines using GPR. In the case of hand-held systems, landmine GPR signatures are generally very unstable and

difficult to characterize [2]. In addition, feedback should be provided to an operator immediately, which implies that a response needs to be produced from the system as soon as any part of a mine has been detected. Thus, mine-detection algorithms for hand-held systems are anomaly detection algorithms that cue operators rather than operate autonomously [2]–[4]. The cues indicate to the operators when a significant change in dielectric has occurred in the subsurface environment. The operator can then interrogate a region of interest and make a decision concerning the presence of a landmine. In this case, constant false alarm rate (CFAR) type algorithms that can account for nonhomogeneous backgrounds have been used very successfully [2], [4]–[8]. These algorithms are generally applied to GPR data that has been adaptively whitened or normalized by principal components transforms [2], [4], [8]. Recently, progress has been made in automating the process of interrogating a region with a hand-held GPR, sometimes in combination with an electromagnetic induction sensor [4], [9]. These systems have been extensively tested on thousands of landmine encounters in a variety of outdoor environments.

For the case of array-based GPR systems fielded on vehicles, it was shown several years ago that feature based methods outperformed energy detectors [10]–[13]. This is generally because radar signal returns are usually significantly corrupted by noise from the ground, clutter, and even the radar itself and the pattern of the signal return from a mine could be distinctive, even if the energy of the signal return from a mine was relatively low. A variety of methods have been used to perform preprocessing of the signal to remove these effects, including wavelets and Kalman filters [14], [15], subspace methods and matching to polynomials [16], subtracting optimally shifted and scaled reference vectors [17], and adaptive extensions of the shift and scale methodology [18].

Among many other approaches to detecting landmines with array-based systems are hidden Markov models (HMM) [19]–[21]. HMMs are stochastic models for complex, nonstationary stochastic processes that produce time sequences of random observations as a function of states, and are widely used for speech recognition and handwriting recognition. In [20] and [21], HMMs are used to model GPR signal returns from both landmines and backgrounds and estimate the likelihood that the signal return is due to landmines. This system has been extensively tested on data collected from thousands of square meters from a variety of outdoor locations.

Recent advances in GPR have resulted in an array-based system that produces data with far less corruption than pre-

Manuscript received June 10, 2004; revised August 18, 2004. This work was supported in part by the U.S. Army under Grants DAAB07-98-D-H752 and DAAB07-98-D-H752.

The authors are with the Department of Computer and Information Science and Engineering, University of Florida, Gainesville, FL 32611 USA (e-mail: pgader@cise.ufl.edu; welee@cise.ufl.edu; jnw@cise.ufl.edu).

Digital Object Identifier 10.1109/TGRS.2004.837333

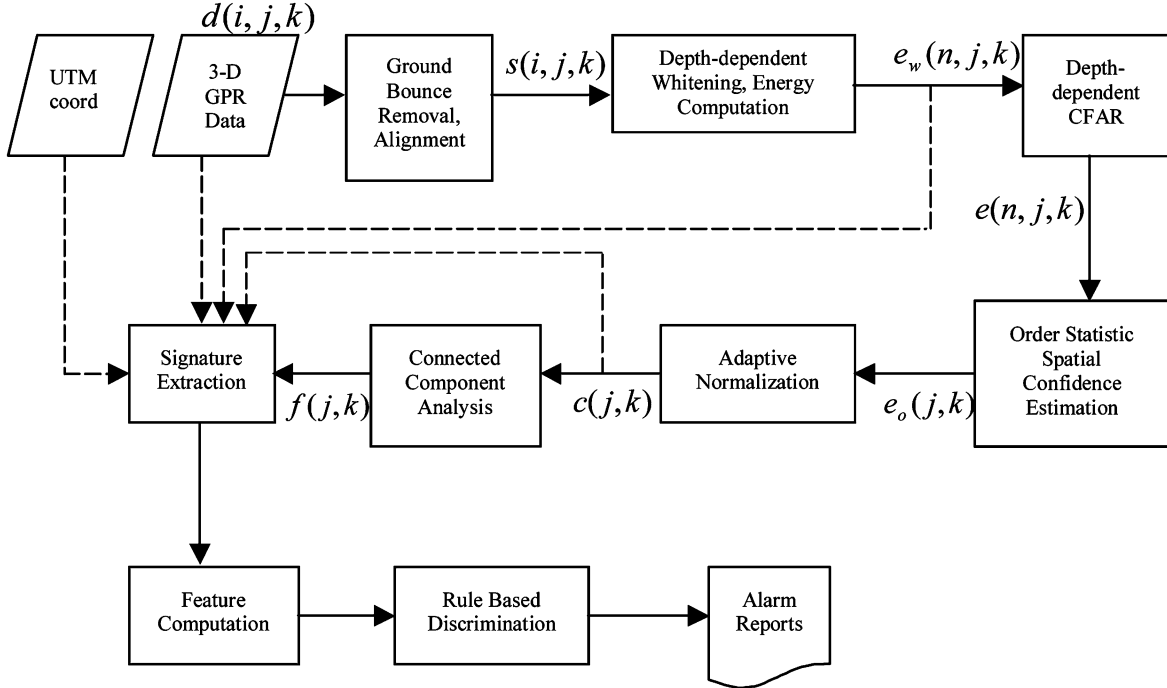


Fig. 1. Block diagram of the FROSAW landmine detection algorithm.

vious systems [22], [23] (see also <http://www.niitek.com>). The characteristics of the data produced by this system imply a new analysis of which algorithms may be most appropriate for array-based mine detection. The proposed detection approach exploits successes in previous extensive landmine detection experiments, while incorporating new, sometimes simpler, concepts. The proposed detection approach uses feature-based rules, order statistics, and adaptive whitening and is, therefore, referred to as the FROSAW method. A specific whitening approach is employed as a component of the approach because of its success shown in [2] where the whitening was applied to frequency-domain data in different frequency bands. In the system proposed here, whitening is applied to time-domain data in different time bands, or depth bins. The concept of using depth bins was proposed by Torrione and Collins [23] who combined it with least mean square processing. In the FROSAW approach, a CFAR algorithm is applied to each of the whitened depth bins. Aggregation of the CFAR outputs is handled in a novel way using order-statistic-like methods. The FROSAW method then exploits several radar-energy based features to detect subsurface anomalies that have mine-like appearance. The problem of aggregating features from several depth and/or frequency bins is a common one in landmine detection (cf. [24]). In this paper, we demonstrate that order-statistic based methods are useful for feature aggregation over depth. The algorithm operates in a quasi-causal fashion and is, thus, suited to a real-time environment. The algorithm involves two primary phases: depth-dependent CFAR anomaly detection and rule-based alarm rejection using depth-dependent features.

FROSAW has been developed and tested on GPR data collected at several different outdoor test sites containing a variety of antitank landmines placed at known locations. In addition, FROSAW has been blind tested on GPR data collected from tens of thousands of square meters of ground at two very different

geographical locations. The blind tests were conducted by an independent agency, and the ground truth (the locations of the mines) was and still is not known to the authors. Although algorithm parameters were developed on calibration lane data, the test data were all run through the same algorithm. The blind test results from both sites were very good and demonstrate the effectiveness of FROSAW for processing time-domain GPR data. Thus, this paper describes a methodology that achieved very high performance on blind tests conducted over tens of thousands of square meters under very different environmental conditions. The method of GPR processing presented here should be of value to those seeking to achieve high performance in landmine detection.

II. ALGORITHM DESCRIPTION

A block diagram of the FROSAW landmine detection algorithm reported is shown in Fig. 1. The input to the process are raw GPR signals sampled by the vehicle-mounted antennas as it travels forward. The Wichmann GPR of NIITEK is used to collect 24 channels of data. Adjacent channels are spaced approximately 5 cm apart in the cross-track direction (see Fig. 2). One scan, defined as the measured waveform that is collected at one downtrack position, is taken at each approximately 5-cm downtrack interval. The signal at each cross-track and downtrack position contains 416 time samples at which the GPR signal return is recorded. Each sample corresponds to approximately 8 ps. Assuming constant velocity, the depth a radar signal travels is proportional to the time that elapses between when the signal is emitted and when the signal return is recorded by the radar, so time and depth are approximately interchangeable variables for indexing the signal traveling along depth. We often refer to the time index as depth, although since the radar wave is traveling

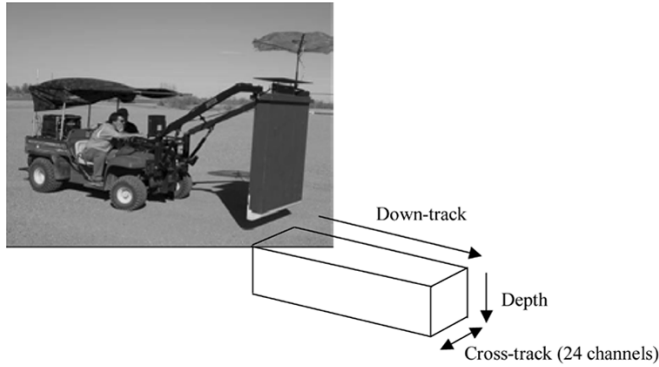


Fig. 2. Picture of the NIITEK/Wichmann GPR. The depth, cross-track, and downtrack directions are also identified.

through different media, this index does not represent a uniform sampling of depth. Thus, we model an entire collection of input data as a three-dimensional (3-D) matrix of sample values $d(i, j, k)$, $i = 1, 2, \dots, I$, $j = 1, 2, \dots, J$, $k = 1, 2, \dots, K$, where the indexes i , j , and k represent depth, cross-track position, and downtrack position, respectively.

In addition, UTM coordinates $x(j, k)$ and $y(j, k)$ associated with scan position are also inputs to the algorithm. The result of our computation is a collection of alarm reports. Each report contains the UTM coordinates of the positions at which the algorithm declares a mine to be present and a confidence value associated with each position.

A. Ground-Bounce Removal and Alignment

In many GPR systems, including the NIITEK/Wichmann GPR, the radar reflection from the ground, or ground bounce, dominates the rest of the signal (see Fig. 3). We exploit this property to identify the location of the ground in the signal as well as to align the ground position in multiple signals. This alignment is necessary because a vehicle-mounted system cannot maintain the radar antenna at a fixed distance above the ground, so the ground location in the signal may change from scan to scan.

To align and then remove the ground bounce, we construct our time-series at each location (j, k) using time-gating. The time-series to be processed starts L time samples after the ground-bounce peak in the measured time-domain signal. Specifically, it is as follows.

```

For every j and k, Do
  i* = arg maxi d(i, j, k)
  s(i, j, k) = d(i + i* + L, j, k)
End
  
```

L is determined based on the length of the ground bounce in time. The reflection from the ground is measured over several time samples, and L is chosen to be 25 time samples so

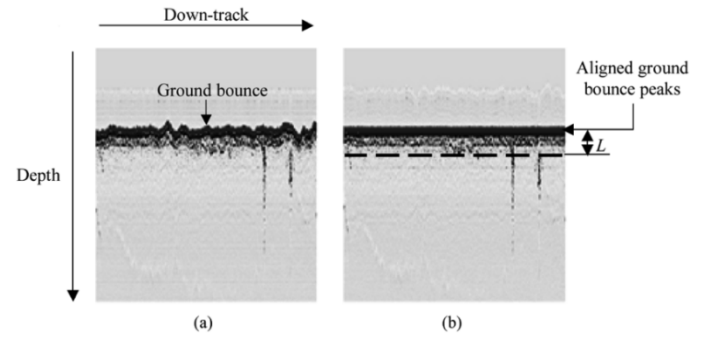


Fig. 3. (a) Vertical slice of raw GPR data. (b) Aligned GPR data with the time-gating line (dashed line) superimposed, where L is the time-gating length.

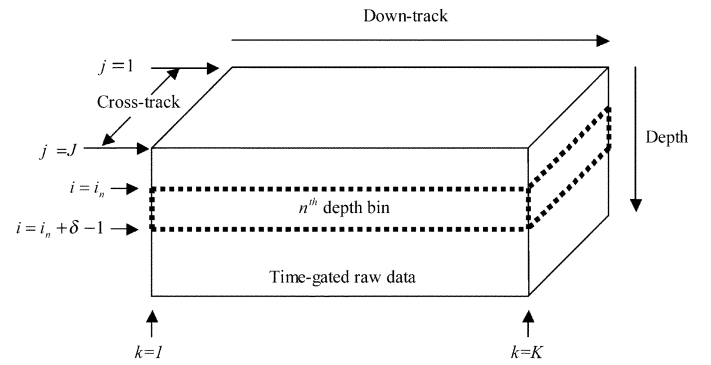


Fig. 4. Dotted data block is the n th depth bin of the time-gated raw data.

that the contribution from the ground is low. The physical distance corresponding to L varies with soil properties but is about 6 cm in air and can vary from 1.5–4 cm in different soils. Several, usually more sophisticated, methods have been applied to the problem of ground-bounce removal, but experimental results indicated that they did not give better performance than time-gating [22].

B. Depth-Dependent Whitening and Energy Computation

After ground-bounce removal, the 3-D data $s(i, j, k)$ are divided into N overlapping depth bins. A depth bin (see Fig. 4) is defined to be a windowed random process obtained by applying the following window function (see (1), shown at the bottom of the page) to the random process $s(i, j, k)$ such that the windowed signal is nonzero only for $i = i_n, i_n + 1, \dots, i_n + \delta - 1$ where i_n is the index of the top edge of the n th window function, and the value δ is a positive integer that represents the number of nonzero time samples for each scan after time-gating. We denote the depth bins of the j th channel as \vec{b}_{nj} , $n = 1, 2, \dots, N$, $j = 1, 2, \dots, J$. Hence, we have NJ random vectors, \vec{x}_{nj} , $n = 1, 2, \dots, N$, $j = 1, 2, \dots, J$, which we refer to as depth bins. To simplify the notations, in the following discussion for the n th depth bin of the j th channel, $n = 1, 2, \dots, N$, $j = 1, 2, \dots, J$, we omit the subscripts n and j and for example use \vec{b} for \vec{b}_{nj} .

$$w_n(i, j, k) = \begin{cases} 1, & i = i_n, i_n + 1, \dots, i_n + \delta - 1, j = 1, 2, \dots, J, k = 1, 2, \dots, k \\ 0, & \text{otherwise} \end{cases} \quad (1)$$

In our experiments, $N = 25$, the overlap between depth bins is 50%, and δ is a variable. The value of δ is computed online using N , the overlap between depth bins, and the size of the samples of time-gating. The value of δ is typically about 10, which roughly corresponds to 0.5–1.6 cm, depending on soil properties.

To reduce noise, decorrelate time samples, and lessen the computational burden, principal component analysis is used to reduce the number of elements in depth bins on a *channel-by-channel* basis. Correlation between channels is not currently used, but since each receiver may have its own statistics, channel-by-channel normalization is appropriate. Let $\vec{b}_{[k]}$ be the k th vector from \vec{b} . Given Q vectors, $\vec{b}_{[k]}, k = 1, 2, \dots, Q$, of the δ -dimensional depth bin \vec{b} , the mean vector $\vec{\mu}$ and $\delta \times \delta$ covariance matrix Σ are estimated by

$$\vec{\mu} = E\{\vec{b}\} \approx \frac{1}{Q} \sum_{k=1}^Q \vec{b}_{[k]} \quad (2)$$

$$\begin{aligned} \Sigma &= E\{(\vec{b} - \vec{\mu})(\vec{b} - \vec{\mu})^T\} \\ &\approx \frac{1}{(Q-1)} \sum_{k=1}^Q (\vec{b}_{[k]} - \vec{\mu})(\vec{b}_{[k]} - \vec{\mu})^T. \end{aligned} \quad (3)$$

Next, the eigenvalues and eigenvectors of Σ are computed. Let the eigenvectors and associated eigenvalues be denoted by \vec{v}_r and $\lambda_r, r = 1, 2, \dots, \delta$, with $\lambda_1 \geq \lambda_2 \geq \dots \geq \lambda_\delta$. The dimensionality is reduced to $m \leq \delta$ dimensions such that only a large percentage (98%) of the energy of the eigenvalues is preserved [2]. The matrix

$$A = \text{diag}(\lambda_1, \lambda_2, \dots, \lambda_m)^{-1/2} [\vec{v}_1, \vec{v}_2, \dots, \vec{v}_m]^T \quad (4)$$

which is called the *whitening matrix* is used to transform \vec{b} to a new random vector $\vec{u}_{[k]}$

$$\vec{u}_{[k]} = A(\vec{b}_{[k]} - \vec{\mu}) \quad (5)$$

and thus $\vec{u}_{[k]}$ is a vector from the whitened depth bin \vec{u} .

After whitening, each depth bin vector $\vec{u}_{[k]} = [u_{[k]1}, u_{[k]2}, \dots, u_{[k]m}]^T$ is first semithresholded, as defined by (6), and its energy is then computed, as defined by (7)

$$z_{[k]i} = \begin{cases} u_{[k]i}, & \text{if } |u_{[k]i}| \geq T \\ 0, & \text{otherwise} \end{cases} \quad (6)$$

$$e_w(n, j, k) = \sum_{i=1}^m z_{[k]i}^2. \quad (7)$$

(Recall that the current discussion is for the n th depth bin of the j th channel.) The threshold T , which is determined empirically, is used to eliminate values that are less than T standard deviations from the mean, since those values are almost certainly from nonmine regions. The mean vectors $\vec{\mu}$ and whitening matrices A are updated only when a certain number (i.e., $Q = 200$) of vectors whose energy is lower than a threshold are accumulated. The choice of Q is based on the observation that the background statistics do not show significant deviations within 200 scans. Upon updating $\vec{\mu}$ and A using (2) and (4), the accumulation starts all over again with zero vector. Features extracted

from the whitened energy signal $\{e_w(n, j, k)\}_{n,j,k}$ are proven to be very useful in discriminating mines and nonmines.

To summarize, for the n th depth bin of the j th channel, the mean and whitening matrix $\vec{\mu}$ and A are updated as follows.

```

Step 1) Initialize  $\vec{\mu}$  and  $A$ . Initialize the mean and standard deviation of the whitened energy signal,  $\mu_e$  and  $\sigma_e$ .
Step 2) Set  $B = \phi$ , and set the number of vectors in  $B$ ,  $N_B$ , to zero.
Step 3)  $k = 1$ .
Step 4) While  $k \leq K$ , Do
  Compute  $u_{[k]} = A(\vec{b}_{[k]} - \vec{\mu})$ .
  Semithreshold  $\vec{u}_{[k]}$  with threshold value  $T$ .
  Compute the energy  $e_w(n, j, k)$ .
  If  $e_w(n, j, k) \leq \mu_e + 3\sigma_e$ , Do
    Put  $\vec{u}_{[k]}$  in  $B$ , and increment  $N_B$  by one.
     $\sigma_e^2 = \alpha_e \sigma_e^2 + (1 + \alpha_e)(e_w(n, j, k) - \mu_e)^2$ 
     $\mu_e = \alpha_e \mu_e + (1 - \alpha_e)e_w(n, j, k)$ 
  End If
  If  $N_B$  equals  $Q$ , Do
    Update  $\vec{\mu}$  and  $A$  using the vectors in  $B$ .
    Clear  $B$ , and set  $N_B = 0$ .
  End If
   $k = k + 1$ .
End While

```

The parameter α_e in Step 4) is a moving average parameter that has a value close to but less than one. (We use 0.9 for α_e .)

As in any adaptive scheme, the statistics must be initialized. Data collection can start at an area where no mines are present. Hence, it is a common assumption that the first few scans of data are target-free. We, therefore, use all the vectors from the 24 channels of the first 24 scans of the n th depth bin to initialize the estimates of $\vec{\mu}$ and A and of μ_e and σ_e of the depth bin. Note that the initialization procedure uses all channels to compute the initial parameter estimates whereas, after initialization, all channels are updated separately. The reason is that only 24 downtrack scans can be used for initialization. Combining all the channels together gives us $24^2 = 576$ samples for initialization as opposed to 24. The instability of the estimates from using only 24 scans was more influential than the difference in statistics between receivers.

C. Depth-Dependent CFAR

Since signal returns from mines usually exhibit high energy contrast to the background and the CFAR value measures local contrast, a CFAR algorithm is applied to each depth bin $\{e_w(n_0, j, k)\}_{j,k}$. That is, for each $n_0 \in \{1, 2, \dots, N\}$, a CFAR algorithm is applied to the 2-D process $\{e_w(n_0, j, k)\}_{j,k}$ as illustrated in Fig. 5. The CFAR algorithm first computes the mean and standard deviation of a comparison region assigned to each point $p = (j_0, k_0)$. The comparison region, composed of a leading comparison region and a trailing comparison region, is constructed in such a way as to better support real-time processing. Since the radar is suspended in front of the vehicle, and there is some distance between the area being scanned

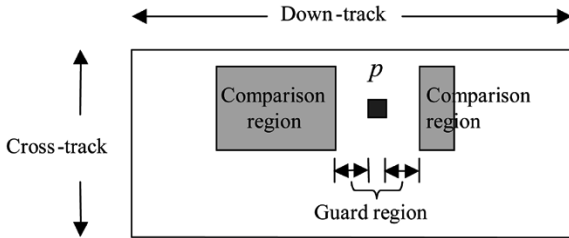


Fig. 5. CFAR comparison and guard regions for the point $p = (j_0, k_0)$. The comparison region on the right needs to be smaller because a decision has to be made to detect a mine before driving over it.

and the front wheel of the vehicle (see Fig. 2), the processing does not have to be strictly causal. In other words, before any declaration must be made for the location in question, more data may be collected along the downtrack direction beyond that location. The background statistics are estimated using points in the comparison region. The CFAR value for each point p is

$$e(n_0, j_0, k_0) = \frac{(e_w(n_0, j_0, k_0) - m_p)}{\sigma_p} \quad (8)$$

where m_p and σ_p are the mean value and standard deviation, respectively, of the points in the comparison region for point p . Guard regions are designed so that points from mines are not included when calculating the background statistics, although this may not be true for mines with large signatures.

D. Order Statistic Spatial Confidence Estimation

The 3-D CFAR values $e(n, j, k)$ need to be projected onto a 2-D confidence map to support declaring alarms at surveyed locations. At each location (j, k) , to count only significant CFAR values, order statistics (OS) operators [25] are used to produce a 2-D confidence map $e_o(j, k)$ from the N depth bins of CFAR values $\{e(n, j, k)\}_{n,j,k}$.

The n th OS of a vector $\vec{\rho} = (\rho_1, \rho_2, \dots, \rho_N)^T$ is the n th smallest element of $\vec{\rho}$. We denote the n th-order statistic by $\rho_{(n)}$ where $\rho_{(1)} \leq \rho_{(2)} \leq \dots \leq \rho_{(N)}$. Let $\rho_n(j_0, k_0) = e(n, j_0, k_0)$, $n = 1, 2, \dots, N$. The 2-D order statistic confidence map is computed as

$$e_o(j_0, k_0) = \left(\sum_{n=N-M+1}^N \rho_{(n)}(j_0, k_0)^2 \right)^{1/2} \quad (9)$$

where M is the number of OS terms included in the computation. This operator computes the energy of the M highest values among the N CFAR values at the point (j_0, k_0) . The reason for using M terms is that, even when a mine is present at (j_0, k_0) , high energy is present only in some of the depth bins.

E. Adaptive Normalization

If the ground properties at different sites were all the same, the 2-D confidence map $e_o(j, k)$ could be directly thresholded to form connected components, and those connected components satisfying empirically predetermined conditions would be reported as alarms. Since ground properties vary from site to

site or even within a site, the appropriate threshold value varies. Hence, we adaptively normalize the confidence map $e_o(j, k)$ so that its values are essentially normally distributed with zero mean and unit variance. After normalization, the confidence map is thresholded with a fixed threshold value.

Consider the confidence values $e_o(j_0, k)$ of channel j_0 . Let $\xi(k) = e_o(j_0, k)$. If no mines are present, the statistics of $\xi(k)$ change relatively slowly. Hence, the mean $\bar{\xi}(k)$ and variance $\sigma_\xi^2(k)$ are estimated recursively by the following exponential averaging [2]

$$\bar{\xi}(k) = \alpha \bar{\xi}(k-1) + (1-\alpha) \xi(k) \quad (10)$$

$$\sigma_\xi^2(k) = \alpha \sigma_\xi^2(k-1) + (1-\alpha)(\xi(k) - \bar{\xi}(k))^2 \quad (11)$$

where α is a moving average parameter that has a value close to but less than unity. (We use 0.8 for α .) The slower the variation of $\xi(k)$, the larger the value of α . The mean $\bar{\xi}(k)$ and variance $\sigma_\xi^2(k)$ are updated only when small $\xi(k)$ is encountered, since they are tracking background statistics. The confidence value is adaptively normalized to get the CFAR output $c(j_0, k)$ as follows:

$$c(j_0, k) = \frac{(e_o(j_0, k) - \bar{\xi}(k))}{\sigma_\xi(k)}. \quad (12)$$

The 2-D CFAR output $c(j, k)$ can now be compared against a fixed threshold value T_c , which is determined empirically.

F. Connected Component Analysis

Connected components are formed by thresholding the 2-D CFAR output with a fixed threshold value T_c . Various properties of each connected component, including area and elongation, which is defined as the ratio of major axis length to minor axis length of the connected component, are computed and used to determine whether to declare the connected component as a mine candidate, i.e., as corresponding to a region at which a mine may be buried. Any connected component that has too small an area or too big an elongation is rejected, i.e., is no longer considered a mine candidate. The minimum area and maximum elongation are experimentally determined. The remaining connected components are reported as candidate alarms with the gray-level centroids of the connected components serving as the alarm locations. The average value of CFAR output inside the connected component is recorded as its CFAR confidence value.

Given an image F with pixel value $f(x, y)$ at point (x, y) , to compute the gray-level centroid, the pixel values are first normalized so that they sum to one, i.e.,

$$\sum_{(x,y) \in F} f(x, y) = 1. \quad (13)$$

Then, the gray-level centroid (x_0, y_0) is computed as

$$x_0 = \sum_{(x,y) \in F} f(x, y) x \quad (14)$$

$$y_0 = \sum_{(x,y) \in F} f(x, y) y. \quad (15)$$

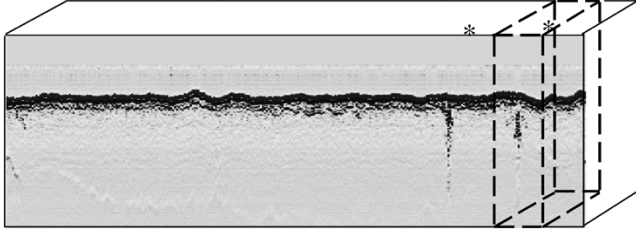


Fig. 6. (Dashed-lined) Block of raw GPR data is extracted and stored for the rightmost reported alarm. Each of the two *'s is the location of an alarm candidate reported by CFAR.

G. Signature Extraction

Each candidate alarm produced by CFAR is further analyzed to reject nonmine-like alarms. Informative features are measured on volumes of GPR data around the CFAR alarm locations and used to discriminate between mines and false alarms. To support the analysis and feature extraction, a *signature* is extracted from the data around an alarm. A signature is defined to be a data structure consisting of the 3-D array of GPR around an alarm location (j_a, k_a) given by $\{d(i, j, k) : i = 1, \dots, I, j = 1, \dots, J, k = k_a - 12, \dots, k_a + 12\}$, together with auxiliary information accumulated in prior processing (see Fig. 6). The auxiliary information includes a portion of the whitened energy signal $\{e_w(n, j, k) : n = 1, \dots, N; j = 1, \dots, J; k = k_a - 12, \dots, k_a + 12\}$ and a region of CFAR output $\{c(j, k) : j = 1, \dots, J; k = k_a - 12, \dots, k_a + 12\}$, as well as the exact position of the alarm in UTM coordinates. From this structure, an alarm can be constructed. We refer to the portions of the whitened energy and CFAR outputs stored in the signature as the whitened energy and CFAR outputs associated with the alarm at location (j_a, k_a) . A collection of signatures is referred to as a signature library.

A signature library is extremely useful for algorithm development. In real-time processing, the signature would not be explicitly created. The algorithm development process uses data collected on calibration, or cal lanes. The UTM coordinates of the mines are available to the algorithm developers on the cal lanes, and it is, therefore, known which alarms correspond to mines and which do not. Thus, distributions of feature values for alarms corresponding to mines and not corresponding to mines can be compared and used to develop algorithms for discriminating mines from nonmines. The reason for extracting and storing signatures of candidate alarms is that various features can be computed for the candidate alarms without requiring the time-consuming process of reading the entire GPR data files, which are quite large. The total size of the raw GPR data files used in the experiments reported here is approximately 41 GB.

H. Feature Computation

It has been consistently observed that in many of the depth bins the whitened energy signal for mines have a compact solid circular shape (sometimes also accompanied with outer rings), while whitened energy signals for false alarms tend to be irregular (see Fig. 7). Based on the above observations, the following features are computed from whitened energy signals for discriminating mines and nonmines.

Compactness: To gauge the compactness of a whitened energy signal, two approaches are taken. Both approaches measure the compactness centered at an alarm location. The first approach is referred to as *adaptive compactness*, whereas the second approach is referred to as *fixed compactness*. Adaptive compactness is defined as the radius from the centroid required for a region of that radius to contain a fixed percentage of the energy of a relatively large radius region. More precisely, let (j_a, k_a) denote the location of the alarm under consideration and let $e_w(n, j, k)$ be the whitened energy associated with the alarm. The whitened energy is normalized as follows:

$$\tilde{e}_w(n, j, k) = \frac{e_w(n, j, k) - \mu_s}{\sigma_s} \quad (16)$$

where μ_s and σ_s are the mean and standard deviation over all whitened energy values associated with the alarm. Denote the normalized whitened energy of the n th depth bin within the disk of radius r by

$$E_n(r; j_a, k_a) = \sum_{(j, k) \in D(r; j_a, k_a)} \tilde{e}_w(n, j, k)^2 \quad (17)$$

where $D(r; j_a, k_a)$ is the disk of radius r centered at alarm location (j_a, k_a) . Let $r_{\max} > 1$ denote a fixed radius and E_p an energy threshold. The adaptive compactness at depth n_0 at location (j_a, k_a) is defined as

$$p_{n_0}(j_a, k_a) = \frac{1}{\min \left\{ r : 1 \leq r \leq r_{\max} \text{ and } \frac{E_{n_0}(r; j_a, k_a)}{E_{n_0}(r_{\max}; j_a, k_a)} \geq E_p \right\}}. \quad (18)$$

Fixed compactness is defined as the ratio of the energy in a 5×5 region to the energy in a 24×25 region, both regions being centered at the reported alarm location in the downtrack direction. That is, the fixed compactness at depth n_0 at location (j_a, k_a) is defined as

$$p_{n_0 f}(j_a, k_a) = \frac{E_{\text{inner}}(j_a, k_a)}{E_{\text{outer}}(j_a, k_a)} \quad (19)$$

where

$$E_{\text{inner}}(j_a, k_a) = \sum_{j=j_a-2}^{j_a+2} \sum_{k=k_a-2}^{k_a+2} \tilde{e}_w(n_0, j, k)^2 \quad (20)$$

$$E_{\text{outer}}(j_a, k_a) = \sum_{j=1}^{24} \sum_{k=k_a-12}^{k_a+12} \tilde{e}_w(n_0, j, k)^2. \quad (21)$$

In general, mines have larger values of compactness than nonmines.

To compute the following features of the normalized, whitened energy signal $\tilde{e}_w(n, j, k)$, the signal is first thresholded by the Otsu thresholding method. Motivated by a conjecture that well-thresholded classes would be separated in gray levels and conversely a threshold giving the best separation of classes in gray levels would be the best threshold, Otsu thresholding method adaptively selects a threshold value

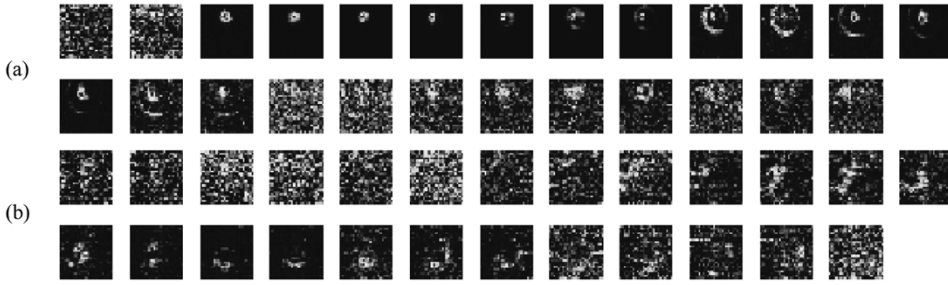


Fig. 7. Depth bins of whitened energy signals for (a) a mine and (b) a nonmine. Note that (a) shows the 25 depth bins of a mine, and (b) shows the 25 depth bins of a false alarm.

to maximize the separability of the gray levels. The Otsu thresholding method is completely described in [26].

For the n_0 th depth bin of the normalized, whitened energy signal $\tilde{e}_w(n, j, k)$, the Otsu threshold T_o is first calculated using $\{\tilde{e}_w(n_0, j, k) : j = 1, \dots, 24, k = k_a - 12, \dots, k_a + 12\}$. Then, $\tilde{e}_w(n_0, j, k)$ is thresholded

$$\tilde{e}'_w(n_0, j, k) = \begin{cases} \tilde{e}_w(n_0, j, k), & \text{if } \tilde{e}_w(n_0, j, k) \geq T_o \\ 0, & \text{otherwise.} \end{cases} \quad (22)$$

After thresholding, connected components are formed. Only the connected component with gray-level centroid closest to the reported alarm location is kept for computing features on the n_0 th depth bin.

Eccentricity: Eccentricity can be thought of as a measure of how much a region resembles a circle. Specifically, the eccentricity of a circle is one. Define for an image F the moment matrix M as

$$M = \begin{bmatrix} m_{xx} & m_{xy} \\ m_{xy} & m_{yy} \end{bmatrix} \quad (23)$$

with

$$m_{xx} = \sum_{(x,y) \in F} f(x,y)(x - x_0)^2 \quad (24)$$

$$m_{yy} = \sum_{(x,y) \in F} f(x,y)(y - y_0)^2 \quad (25)$$

$$m_{xy} = \sum_{(x,y) \in F} f(x,y)(x - x_0)(y - y_0) \quad (26)$$

where (x_0, y_0) is the gray-level centroid of F . Let λ_1 and λ_2 be the eigenvalues of the matrix M satisfying $\lambda_1 \geq \lambda_2 > 0$. Then, the eccentricity of the image F is defined as

$$e_F = \frac{\lambda_2}{\lambda_1}. \quad (27)$$

The image F in our calculation is the Otsu-thresholded normalized whitened energy signal with lone connected component whose gray-level centroid is closest to the reported alarm location. This same image is used for computing each of the following features.

Solidity: Solidity is the proportion of the pixels in the convex hull that are also in the region, where a convex hull is defined as the smallest convex polygon that can contain the region. See Fig. 8 for examples.

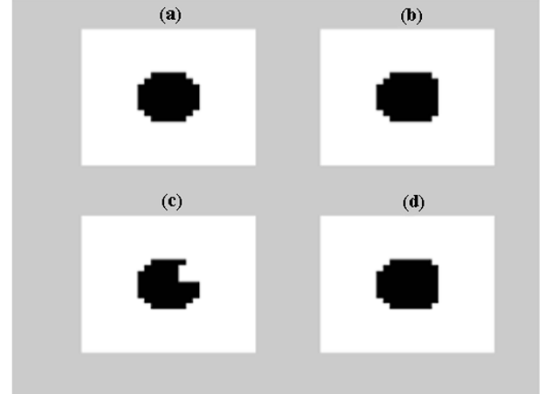


Fig. 8. (a) Original image. (b) Convex hull of the image in (a). (c) Another original image. (d) Convex hull of the image in (c).

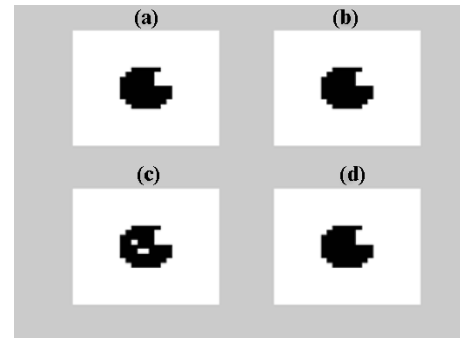


Fig. 9. (a) Original image. (b) Filled image of the image in (a). (c) Another original image. (d) Filled image of the image in (c).

Ratio of Area to Filled Area: The filled image of an image F is F itself with all its holes filled in. The filled area of F is defined as the area of the filled image of F . Because holes are usually not expected to be present in the image of the whitened energy signal of a mine, the ratio of area to filled area of an image is a good indicator as to whether a mine is present. See Fig. 9 for examples.

I. Rule-Based Discrimination

The following rules were established for discriminating mines and nonmines based on observations of feature distributions. The fixed compactness values of the whitened energy signals are computed for each depth bin, and those three depth bins with highest three fixed compactness values are used to compute the aforementioned features. Thus, three values for each feature will be available for use for each reported

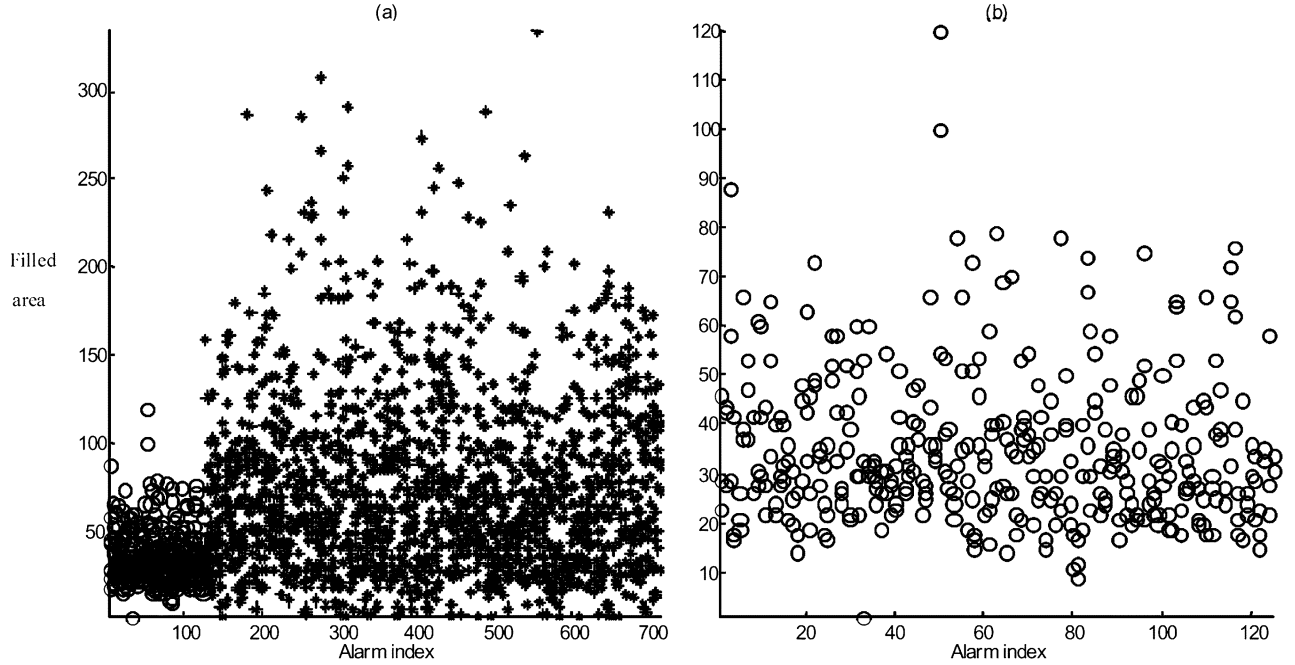


Fig. 10. Filled areas of whitened energy signal for mines and nonmines. (a) o: mines, *: nonmines. (b) o: mines.

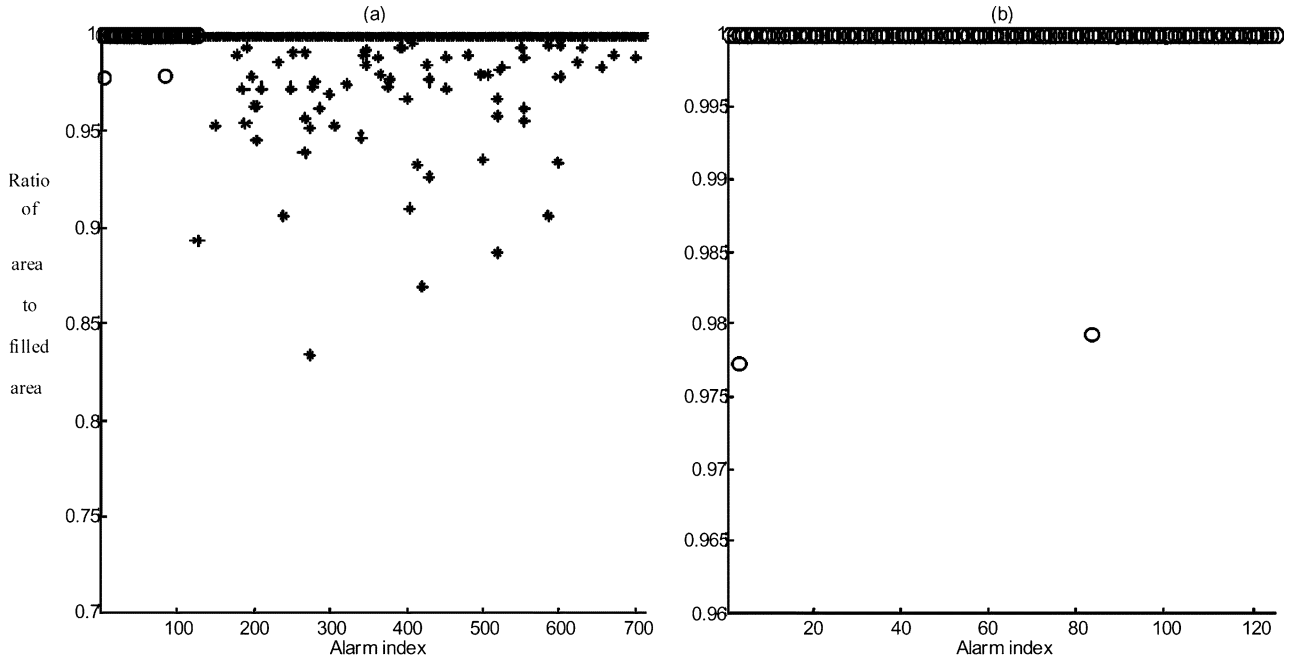


Fig. 11. Ratio of area to filled area of whitened energy signal for mines and nonmines. (a) o: mines, *: nonmines. (b) o: mines.

alarm. More precisely, the fixed compactness is computed for each depth bin of the normalized whitened energy signal, i.e., $p_{nf}(j_a, k_a)$ is determined for $n = 1, 2, \dots, N$. Suppose $p_{n_1f}(j_a, k_a) \geq p_{n_2f}(j_a, k_a) \geq \dots \geq p_{n_Nf}(j_a, k_a)$. That is, the n_1 th, n_2 th, and n_3 th depth bins have the largest three fixed compactness values. Then, an image F is obtained by getting from the n_1 th depth bin the Otsu-thresholded normalized whitened energy signal with lone connected component whose gray-level centroid is closest to the reported alarm location. Several features including area, filled area, and solidity, are next computed of the image F . The same procedure is applied to the n_2 th and n_3 th depth bins.

The following rules were devised so as to reject only false alarms in the training data. For easy reference, scatter plots of the features are given in Figs. 10–12. Note that, in each of Figs. 10–12, (b) is a zoomed display of only the mine features from (a). Based on Fig. 10, which shows that some of the nonmines have larger filled areas than all the mines, the following rules are established.

- Rule 1. If any filled area is larger than T_1 , reject the alarm.
- Rule 2. If more than one of the filled areas are larger than T_2 , reject the alarm.

The values T_1 and T_2 were determined so that no mines will be rejected by Rule 1 and/or Rule 2 in the training set. Rules 1

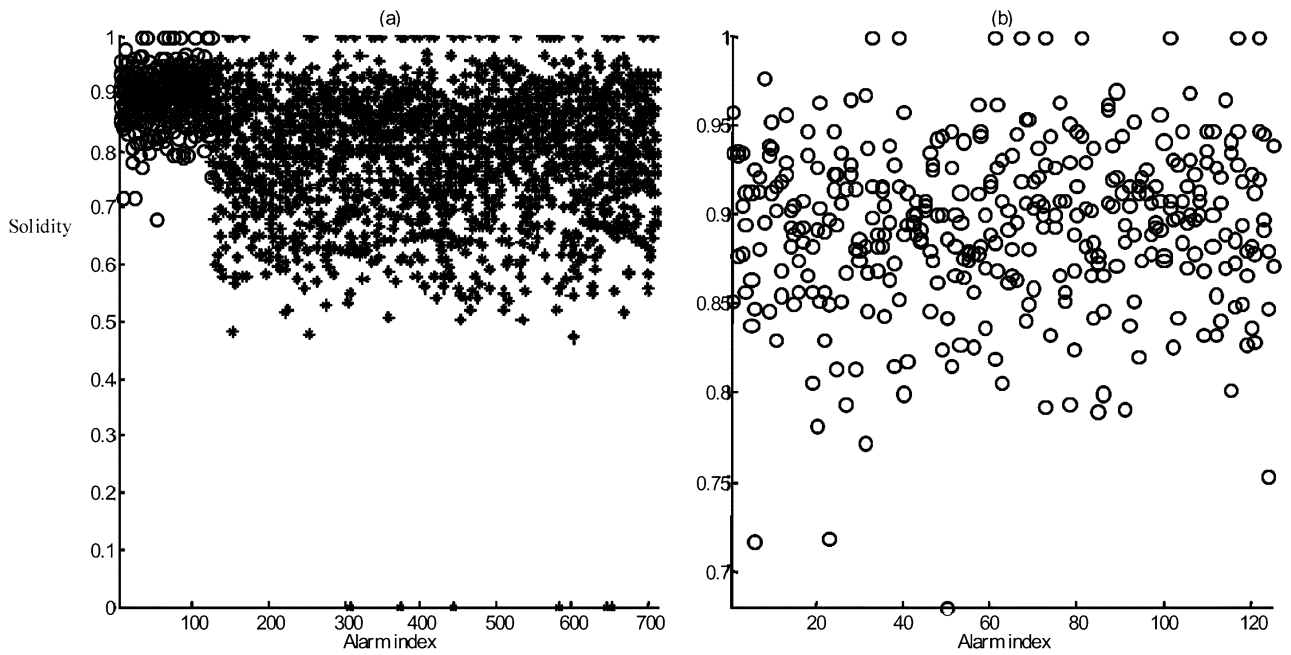


Fig. 12. Solidities of whitened energy signal for mines and nonmines. (a) \circ : mines, $*$: nonmines. (b) \circ : mines.

and 2 imply that all three filled areas of a mine cannot exceed the upper limit T_1 and only one out of three areas can be as big as T_2 . The rationale for these rules is that areas of regions due to mines can only be within a certain range due to the physical sizes of mines.

Based on Fig. 11, which shows that in the training set the ratio of area to filled area is close to one for every mine, the following rules are established.

- *Rule 3.* If any ratio of area to filled area is less than T_3 , reject the alarm.
- *Rule 4.* If more than one of the ratios of area to filled area are less than T_4 , reject the alarm.

The lower limits T_3 and T_4 are set so that almost no mines will be rejected on the training set.

Based on Fig. 12, the following rules are established.

- *Rule 5.* If any solidity is less than T_5 , reject the alarm.
- *Rule 6.* If more than one of the solidities are less than T_6 , reject the alarm.

After whitening, mines generally have a continuously high response across the area of a mine, leading to solid connected components. Hence, solidity is expected to be high for mines.

The threshold values used to generate the experimental results given here are $T_1 = 140$, $T_2 = 115$, $T_3 = 0.96$, $T_4 = 0.99$, $T_5 = 0.6$, and $T_6 = 0.78$.

As noted in [28], the product of CFAR and adaptive compactness provides effective discrimination information (although adaptive compactness in [28] is the inverse of adaptive compactness here). Furthermore, analysis of training data show that a linear discriminator would reject even more false alarms if eccentricity and the adjusted CFAR value were used as inputs to the discriminator. A plot of eccentricity versus adjusted CFAR confidence value is given in Fig. 13. The superimposed straight line in Fig. 13, whose intercept is 0.25 and slope is -0.02 is used to define a linear discriminator with the property that every point lying on the same side of the line as the origin

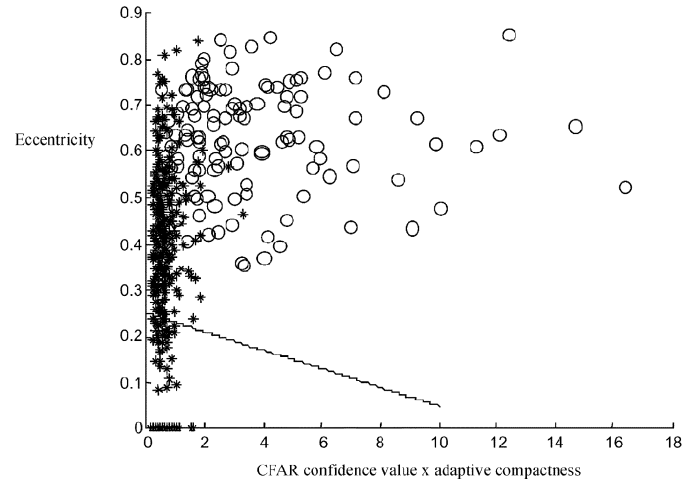


Fig. 13. Plot of eccentricity versus CFAR confidence value \times adaptive compactness where \circ represents mines, and $*$ represents nonmines.

(0,0) is assigned a final confidence value of zero, and all of the points lying on the other side keep their adjusted CFAR confidence value (i.e., CFAR confidence value multiplied by adaptive compactness). The intercept and slope of the line were chosen conservatively based on the calibration data to better accommodate deviations of features of test data from those of the calibration data.

It should be mentioned that other, less ad hoc, methods of combining these features that did not use order statistics or rules were intensely investigated but they did not lead to improved performance beyond using the CFAR values. Other less ad hoc methods of combining these features, including relevance vector machine (RVM) [27] and k-means clustering, were investigated. The RVM is a machine-learning scheme within a probabilistic framework that builds models with sparse parameters from large sets of training data. The well-known k-means clustering has an obvious advantage with its computational simplicity. These less

TABLE I
NUMBER OF METAL AND PLASTIC CASED MINES AND MINE SIMULANTS ON THE CALIBRATION LANES. LANE 2C ALSO HAD 32 EMPLACED CLUTTER ITEMS SUCH AS PIECES OF METAL AND WOOD AS WELL AS HOLES THAT WERE DUG OUT AND FILLED IN

	Lane 1A	Lane 1B	Lane 1C	Lane 2A	Lane 2B	Lane 2C
Metal	4	4	4	4	4	0
Plastic	14	14	16	10	10	11
Clutter	0	0	0	0	0	32
Holes	0	0	0	0	0	7

ad hoc methods did not perform as well as the feature-based rules.

III. EXPERIMENTAL RESULTS

Two sets of experiments were performed. The FROSAW algorithm was developed on GPR collected from outdoor test lanes at two different locations. The first location, site 1, was a temperate region with significant rainfall whereas the second region, site 2, was a desert region. Soil was moist at site 1, and very dry at site 2. The lanes are simulated roads. There are two types of lanes: lanes for which the locations of the mines are known and lanes for which the locations of the mines are not known. The first type of lane is called a calibration lane and the second type is called a blind lane. The calibration and blind lanes at site 1 are 500 m long and 3 m wide. The calibration lanes at site 2 are 300 m long and 3 m wide. The blind lanes at site 2 are 1200 m long and 3 m wide. The calibration lanes at site 1 are labeled 1A, 1B, and 1C and have mines only. The calibration lanes at site 2 are labeled lanes 2A, 2B, and 2C. Lanes 2A and 2B have mines only and lane 2C has mines and emplaced clutter items, such as pieces of metal and wood. The number of mines of each type in the calibration areas is given in Table I. All the mines are Anti-Tank (AT) mines.

Two calibration lane data collections were performed at each site. The collections at site 1 were made in November and December 2002 and the collections at site 2 were made in October 2002 and January 2003. In order to place them in tables easily, we refer to the earliest collection at each location as collection 1 and the later collection as collection 2. The blind testing was performed at site 1 in May 2003 and at site 2 in January 2003. Because moisture level and thus dielectric of the soil affect the radar responses, data collected from different dates/sites is generally different. Those parameters were neither called for by the presented algorithm nor measured, though.

The detection algorithm is scored in terms of probability of detection (PD) versus false alarm rate (FAR). As is usual, confidence values are thresholded at different levels to produce receiver operating characteristic (ROC) curves. For a given threshold, a mine is detected if there is an alarm within 0.25 m from the edge of the mine with confidence value above the threshold. Given a threshold, the PD for a lane or set of lanes is defined to be the number of mines detected divided by the number of mines. A false alarm is an alarm with confidence above the threshold and with location farther than 0.25 m from the edge of any mine. The FAR is defined as the number of false alarms per square meter.

TABLE II
PD VERSUS FAR ON CALIBRATION LANES

Lane	PD (%)	Collection 1		Collection 2	
		CFAR	FROSAW	CFAR	FROSAW
Lane 1A	78-83	0.0147	0.0007	0.0027	0.0007
	84-88	0.0287	0.0053	0.0053	0.0007
	89-94	0.0433	0.0080	0.0327	0.0080
	95-100	N/A	N/A	N/A	N/A
Lane 1B	84-88	0.0167	0.0020	0.0087	0.0013
	89-94	0.0200	0.0030	0.0107	0.0013
	95-100	0.0207	0.0040	0.0120	0.0020
Lane 1C	86-90	0.0073	0.0007	0.0193	0.0073
	91-95	0.0140	0.0013	0.0633	0.0073
	96-100	0.0147	0.0047	0.0787	0.0160
Lane 2A	80-86	0.0022	0.0011	0	0
	87-93	0.0022	0.0011	0	0
	94-100	0.0044	0.0022	0	0
Lane 2B	79-85	0.0011	0	0	0
	86-92	0.0022	0	0.0022	0
	93-100	0.0465	0.0119	0.0335	0.0011
Lane 2C	73-81	0.0428	0.0271	0.0473	0.0304
	82-90	0.0507	0.0271	0.0519	0.0304
	91-100	N/A	0.0282	0.0575	0.0338

TABLE III
EXAMPLES OF SCORES OBTAINED BY THE ALGORITHMS IN [10]

Choquet		Sugeno	
PD (%)	FAR	PD (%)	FAR
82	0.008	73	0.006
84	0.009	73	0.006
85	0.010	75	0.007
88	0.013	82	0.008
89	0.016	86	0.009
90	0.020	89	0.013
91	0.023	89	0.013
91	0.028	91	0.015
92	0.032	97	0.046
92	0.036	97	0.046

Table II shows PD versus FAR from the calibration lanes. For each lane, a range of PD values is given and the corresponding false alarm rates obtained by just using the CFAR output and by using the full rule-based FROSAW algorithm are presented. As can be seen, FARs of FROSAW are better than FARs of CFAR. In addition, the FARs for CFAR are more variable than those of FROSAW. Note that although CFAR stands for Constant FAR, it will only be the case when the distributional assumptions are met, and they are not met here. We attribute this to the fact that FROSAW is feature based. As you move from top to bottom through the rows in the table corresponding to a specific lane, each row corresponds to one more mine. Small differences in environmental conditions may make the more difficult mines slightly harder to detect, leading to more false alarms. Notice that at site 1, since the lanes are 500 m long by 3 m wide, one false alarm represents a FAR of $1/1500 \approx 0.0007$ and at site 2, one false alarm represents a FAR of $1/900 \approx 0.0011$.

For more comparison, scores obtained by algorithms in [10] are given in Table III, where various features are fused by Choquet and Sugeno fuzzy integrals to generate final confidence values for the calibration site at Fort A.P. Hill, VA. Because scores obtained by FROSAW and other algorithms are not for the same sites, only intuitive comparisons can be made as follows. For FROSAW, the FAR at any PD is the average of FARs

TABLE IV
AVERAGE REDUCTION OF FARs BY FROSAW OVER THE ALGORITHMS IN [10]

	Site 1		Site 2	
	Collection 1	Collection 2	Collection 1	Collection 2
Choquet	76%	71%	97%	100%
Sugeno	71%	62%	95%	100%

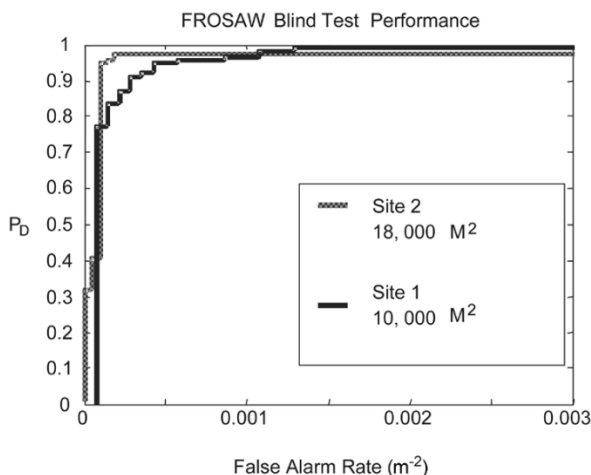


Fig. 14. Results on blind tests.

at that PD among lanes for one collection. Note that lane 2C is excluded in the comparisons because only lane 2C has emplaced clutters. For Choquet and Sugeno, the FAR for any PD is the lowest FAR achievable at that PD. And, when comparing any two algorithms, only FARs at achievable PDs for both algorithms are taken into consideration. The average reductions of FAR by the system described here over the ones described in [10] are listed in Table IV. It can be seen that the results reported here are much better, and it is also true when comparison is made to other previously reported systems [12], [13], [20], [21].

Scores on the blind tests were compiled by an independent institution. The location, number, and type of mines are unknown to us. We were provided with the data, applied the algorithms, and supplied alarm locations with confidence to the independent institution. We assumed that the distribution of mines in the blind lanes was similar to that of the calibration lanes. The institution supplied us with ROC curves. The ROC curves are shown in Fig. 14.

On the calibration lane data, applying Rules 1–6 rejected 129 of 288 false alarms for collection 1 of site 1, 159 of 332 for collection 2 of site 1, 185 of 531 for collection 1 of site 2, and 157 of 448 for collection 2 of site 2. Rules 1–6, in spite of their simplicity, reject a high percentage of false alarms. Again, the threshold values in Rules 1–6 were chosen conservatively based on the calibration data in order to accommodate test data. The effect of the rules on the blind test is unknown, since the authors no longer have the ground truth. In fact, the authors no longer have the GPR data from site 2, since they were not allowed to keep the data after the test was completed.

Several improvements to the algorithm are under investigation using calibration lane data. To determine if a declaration

must be made at any location, the 2-D CFAR map is first thresholded to form connected components. It has been observed that thresholding against a fixed threshold value remove descriptive characteristics of the CFAR map. An example is given in Fig. 15, where (a) is 24×25 CFAR map for the alarm corresponding to a clutter object (metal sheet), and (b) is the CFAR map in (a) thresholded against a fixed threshold value 0.7. The CFAR map in (a) clearly exhibits a hollow core, which could be a discriminating feature. However, that characteristic is not preserved in (b) after thresholding. One viable alternative is to threshold the CFAR map against adaptive threshold values, e.g., Otsu threshold. The CFAR map thresholded against the Otsu threshold is shown in (c), and features extracted from this thresholded map are expected to characterize the clutter better than the one in (b). Adaptive thresholding methods as well as methods based on multiple thresholds, such as continuous Choquet integration [29], are currently under investigation.

Another area for potential improvement is selection of depth bins for feature analysis. For each reported alarm, features extracted from three depth bins of whitened energy signal that have the highest three fixed compactness values are used for discrimination. Using only fixed compactness may not be the best scheme for selecting depth bins from which features are extracted. An example is given in Fig. 16, where the 25 depth bins of whitened energy signal of a clutter object (a different metal sheet) are shown. As we base our selection upon only fixed compactness, we pick for feature computation those depth bins marked with “1”, “2”, and “3” corresponding to the highest, the second highest, and the third highest compactnesses, respectively. However, features extracted from the first few depth bins might best characterize the clutter. We have been looking into novel architectures based on optimized order statistic operators for picking depth bins without the need of predetermined selection criteria.

IV. CONCLUSION

An algorithm for detecting landmines using feature-based rules, adaptive whitening, and order statistics has been described and applied to the Wichmann GPR fielded by NIITEK incorporated. The performance of the algorithm with this GPR is quite good. The adaptive whitening in the time domain and use of order statistics are novel methods that improved performance considerably. Feature-based rules outperformed other techniques. The scores on calibration lanes with emplaced clutter were not as good as on other lanes, but they were still as good as many recently published scores obtained from data without clutter, cf. [10], [12], [13], [20], and [21].

The results presented in this paper, and by others [23], demonstrate that very low FAR at high PD can be achieved for those lanes with no emplaced clutter. It is considered a high level of success on landmine detection when only a small number of false alarms are reported over lanes of hundreds of square meters. On the other hand, lanes with emplaced clutter, e.g., lane 2C, pose difficult challenges because signal returns from clutter objects possess characteristics that are similar in some aspects to those of signal returns from mines. Because of the tremendous amount of data that needs to be investigated on and the

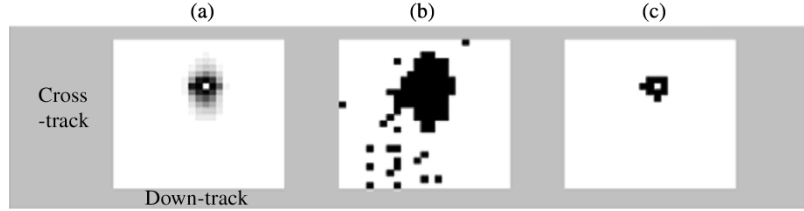


Fig. 15. (a) Two-dimensional CFAR map. (b) CFAR map thresholded against a fixed threshold value, 0.7. (c) CFAR map thresholded against Otsu threshold.

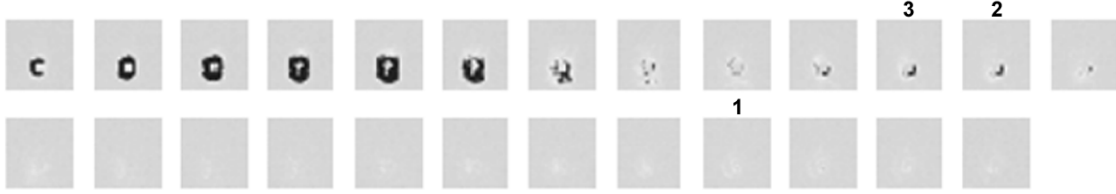


Fig. 16. Depth bins of whitened signal energy for a clutter object (metal sheet). Note that the scale is different from that of Fig. 8 to make the pattern clearer.

success of achieving low FAR at high PD for lanes without emplaced clutters, the focus on GPR-based landmine detection algorithms should shift from simply detecting mines to discriminating between mines and clutter objects, at least for the case of AT mines.

ACKNOWLEDGMENT

The authors thank D. Reidy and C. Lee (U.S. Army Humanitarian Demining Office) and R. Weaver (U.S. Army Counter-mine Division) for their support of this work. The authors also thank L. Collins, P. Torrione, and S. Throckmorton (Duke University) and F. Clodfelter and S. Frasier (NIITEK) for their technical discussions, insights, and cooperation.

REFERENCES

- [1] P. Stott, "The UTM grid reference system," *J. Soc. Indust. Archeol.*, vol. 3, no. 1, pp. 1–14, 1977.
- [2] K. C. Ho and P. D. Gader, "A linear prediction land mine detection algorithm for hand held ground penetrating radar," *IEEE Trans. Geosci. Remote Sensing*, vol. 40, pp. 1374–1384, June 2002.
- [3] J. Staszewski and A. Davison, "Mine detection training based on expert skill," *Proc. SPIE*, vol. 4038, pp. 90–101, Apr. 2000.
- [4] K. C. Ho, L. M. Collins, L. G. Huettel, and P. D. Gader, "Discrimination mode processing for EMI and GPR sensors for hand-held land mine detection," *IEEE Trans. Geosci. Remote Sensing*, vol. 42, pp. 249–263, Jan. 2004.
- [5] P. P. Gandhi and S. A. Kassam, "Analysis of CFAR processors in nonhomogeneous background," *IEEE Trans. Aerosp. Electron. Syst.*, vol. 24, July 1988.
- [6] E. Conte, A. De Maio, and C. Galdi, "Signal detection in compound-gaussian noise: Neyman-Pearson and CFAR detectors," *IEEE Trans. Signal Processing*, vol. 48, pp. 419–428, Feb. 2000.
- [7] R. Srinivasan, "Simulation of CFAR detection algorithms for arbitrary clutter distributions," *Proc. Inst. Elect. Eng.*, vol. 147, pp. 31–40, Feb. 2000.
- [8] S. Yu, R. K. Mehra, and T. R. Witten, "Automatic mine detection based on ground penetrating radar," *Proc. SPIE*, vol. 3710, pp. 961–972, Apr. 1999.
- [9] K. C. Ho, J. Devaney, and P. D. Gader, "Feature-based processing for hand-held landmine detector," *Proc. SPIE*, vol. 4742, Apr. 2002.
- [10] S. Yu, A. Gandhi, and T. R. Witten, "Automatic mine detection based on multiple features," *Proc. SPIE*, vol. 4038, Apr. 2000.
- [11] P. D. Gader and J. M. Keller, "Multi-Sensor fusion with DARPA backgrounds data," in *Proc. SPIE*, vol. 3392, Apr. 1998.
- [12] P. D. Gader, J. M. Keller, and B. N. Nelson, "Recognition technology for the detection of buried land mines," *IEEE Trans. Fuzzy Syst.*, vol. 9, pp. 31–43, Feb. 2001.
- [13] P. D. Gader, B. Nelson, H. Frigui, G. Vaillette, and J. Keller, "Fuzzy logic detection of landmines with ground penetrating radar," *Signal Process.*, vol. 80, no. 6, pp. 1069–1084, June 2000.
- [14] D. Carevic, "Clutter reduction and target detection in ground penetrating radar data using wavelets," *Proc. SPIE*, vol. 3710, pp. 973–978, Apr. 1999.
- [15] ———, "Kalman filter-based approach to target detection and target-background separation in ground-penetrating radar data," *Proc. SPIE*, vol. 3710, pp. 1284–1288, Apr. 1999.
- [16] A. Gunatilaka and B. A. Baertlein, "Subspace decomposition technique to improve GPR imaging of anti-personnel mines," *Proc. SPIE*, vol. 4038, Apr. 2000.
- [17] H. Brunzell, "Detection of shallowly buried objects using impulse radar," *IEEE Trans. Geosci. Remote Sensing*, vol. 37, pp. 875–886, Mar. 1999.
- [18] R. Wu, A. Clement, J. Li, E. G. Larsson, M. Bradley, J. Habersat, and G. Maksymenko, "Adaptive ground bounce removal," *Electron. Lett.*, vol. 37, no. 20, pp. 1250–1252, Sept. 2001.
- [19] O. Löhllein and M. Fritzsche, "Classification of GPR data for mine detection based on hidden markov models," in *EUREL Conf. Detection of Abandoned Landmines*, Edinburgh, U.K., Oct. 1998.
- [20] P. D. Gader, M. Mystkowski, and Y. Zhao, "Landmine detection with ground penetrating radar using hidden Markov models," *IEEE Trans. Geosci. Remote Sensing*, vol. 39, pp. 1231–1244, June 2001.
- [21] Y. Zhao, P. D. Gader, P. Chen, and Y. Zhang, "Training DHMMS of mine and clutter to minimize landmine detection errors," *IEEE Trans. Geosci. Remote Sensing*, vol. 41, pp. 1016–1024, May 2003.
- [22] L. M. Collins, P. A. Torrione, V. S. Munshi, C. S. Throckmorton, Q. E. Zhu, J. F. Clodfelter, and S. Frasier, "Algorithms for landmine detection using the NIITEK ground penetrating radar," *Proc. SPIE*, vol. 4742, pp. 709–718, Aug. 2002.
- [23] L. M. Collins, P. A. Torrione, C. S. Throckmorton, X. Liao, Q. E. Zhu, Q. Liu, L. Carin, F. Clodfelter, and S. Frasier, "Algorithms for landmine discrimination using the NIITEK ground penetrating radar," *Proc. SPIE*, vol. 5089, Apr. 2003.
- [24] A. K. Hocaoglu, P. D. Gader, J. M. Keller, and B. N. Nelson, "Anti-Personnel land mine detection and discrimination using acoustic data," *J. Subsurf. Sens. Technol. Appl.*, vol. 3, no. 2, pp. 75–93, Apr. 2002.
- [25] I. Pitas and A. N. Venetsanopoulos, "Order statistics in digital image processing," *Proc. IEEE*, vol. 80, pp. 1893–1921, Dec. 1992.
- [26] N. Otsu, "A threshold selection method from gray-level histograms," *IEEE Trans. Syst. Man Cybern.*, vol. SMC-9, pp. 62–66, Jan. 1979.
- [27] M. E. Tipping, "Sparse Bayesian learning and the relevance vector machine," *J. Mach. Learn. Res.*, no. 1, pp. 211–244, 2001.
- [28] P. D. Gader, J. N. Wilson, and W.-H. Lee, "Adaptive whitening for landmine detection with array-based ground penetrating radar," in *Proc. Int. Conf. Requirements Technologies for Detection, Removal, and Neutralization of Landmines and UXO (EUDEM 2003)*, Sept. 15–18, 2003, pp. 509–515.
- [29] P. D. Gader, W.-H. Lee, and A. Mendez-Vasquez, "Continuous choquet integrals with respect to random sets with applications to landmine detection," in *Proc. IEEE Conf. Fuzzy Systems*, July 2004.



Paul D. Gader (M'87-SM'99) received the Ph.D. degree in mathematics for parallel image processing and applied mathematics research from the University of Florida, Gainesville, in 1986.

He was a Senior Research Scientist with Honeywell's Systems and Research Center, a Research Engineer and Manager at the Environmental Research Institute of Michigan (ERIM), and a faculty member at the University of Wisconsin, the University of Missouri, and the University of Florida, where he is currently a Full Professor in the Department of Computer and Information Science and Engineering. He has been active in land mine detection algorithm research since 1996. He has led teams that devised and tested several real-time algorithms in the field for mine detection. He served as Technical Director of the University of Missouri MURI on Humanitarian Demining for two years. He is currently involved in several landmine detection projects including hand-held and ground-based mine detection systems, acoustic mine detection, detection of trip-wires, and is a member of a new MURI team investigating the science of land target spectral signatures. He has authored over 150 technical publications in the areas of image and signal processing, applied mathematics, and pattern recognition, including over 50 refereed journal articles.

Wen-Hsiung Lee received the B.S. degree in electronics engineering from National Chiao-Tung University, Hsinchu, Taiwan, R.O.C., in 1990, and the M.S. and Ph.D. degrees from the University of Florida, Gainesville, in 1994 and 2001, respectively.

Since 2002, he has been a Post-Doctoral researcher with the Department of Computer and Information and Engineering, University of Florida.

Joseph N. Wilson received the B.S. degree in applied mathematics with the emphasis on computer science from Florida State University, Tallahassee, in 1977, the M.S. degree in applied mathematics and computer science in 1980 and the Ph.D. in computer science in 1985, both from the University of Virginia, Charlottesville.

Since 1984, he has been on the faculty of the Computer and Information Science and Engineering Department at the University of Florida, Gainesville, where he served as Associate Chair from 1994 to 2001. His research interests include computer vision, image processing, programming languages, and file systems.